

Nearly Polar orbit of the sub-Neptune HD3167 c

Constraints on a multi-planet system dynamical history

S. Dalal¹, G. Hébrard^{1,2}, A. Lecavelier des Étangs¹, A. C. Petit³, V. Bourrier⁴, J. Laskar³, P.-C. König¹, A.C.M. Correia^{5,3}

¹ Institut d'astrophysique de Paris (IAP), UMR7095 CNRS, Université Pierre & Marie Curie, 98bis Boulevard Arago, 75014 Paris

² Observatoire de Haute-Provence (OHP), CNRS, Université d'Aix-Marseille, 04870, Saint-Michel-l'Observatoire, France

³ IMCCE, CNRS-UMR 8028, Observatoire de Paris, PSL University, Sorbonne Université, 77 Avenue Denfert-Rochereau, 75014 Paris, France

⁴ Observatoire de l'Université de Geneve, 51 chemin des Maillettes, Versoix, Switzerland.

⁵ CFisUC, Department of Physics, University of Coimbra, 3004-516 Coimbra, Portugal.

June 22, 2022

ABSTRACT

Aims. We present the obliquity measurement i.e. the angle between the normal of the planet orbital plane and stellar spin axis of the sub-Neptune planet HD3167 c that transits a bright, nearby K0 star. New observations obtained with HARPS-N at Telescopio Nazionale Galileo (TNG) are employed for our analysis. We study the orbital architecture of this multi-planet system to understand its dynamical history. We also put constraints on the obliquity of planet d from the geometry of the planetary system and the dynamical study of the system.

Methods. The sky-projected obliquity is measured using three different methods, i.e. Rossiter-McLaughlin anomaly, Doppler tomography and Reloaded Rossiter-McLaughlin techniques. We perform the stability analysis of the system and investigate the dynamical interactions between the planets and star.

Results. HD3167 c is found to be nearly polar with sky-projected obliquity, $\lambda = -98^\circ \pm 23^\circ$. This misalignment of the orbit of planet c with the spin axis of the host star is detected with 97% confidence. The analysis of the dynamics of this system yields coplanar orbits of planets c and d. It also shows that it is unlikely that the currently observed system can, by itself, generate such a large obliquity for planets c and d. However the polar orbits of planets c and d could be explained by the presence of an outer companion in the system. Follow-up observations of the system are required to confirm such a long period companion.

Key words. Techniques: radial velocities – planets and satellites: fundamental parameters – planets and satellites: individual (HD3167) – Planet-star interactions

1. Introduction

Obliquity is defined as the angle between the normal of a planetary orbit and the planet host star rotation axis. It is an important probe to understand the dynamical history of the exoplanetary systems. Solar system planets are nearly aligned with obliquities less than 7° , which might be a consequence of their formation from the protoplanetary disk. However, this is not the case for all exoplanetary systems. Various misaligned systems i.e. $\lambda \gtrsim 30^\circ$ including some retrograde ($\lambda \sim 180^\circ$, e.g., Hébrard et al. 2008) or nearly polar ($\lambda \sim 90^\circ$, e.g., Triaud et al. 2010) orbits have been discovered. These misaligned orbits may result from Kozai migration, and/or tidal friction (Nagasawa et al. 2008; Fabrycky & Tremaine 2007; Guillochon et al. 2011; Correia et al. 2011) where the close-in planets migrate due to scattering, or early-on interaction between the magnetic star and its disc (Lai et al. 2011), or later from elliptical tidal instability (Cébron et al. 2011). Other possibility can be that the star has been misaligned since the days when the protoplanetary disk was present due to inhomogeneous

accretion (Bate et al. 2010) or a stellar flyby (Batygin & Konstantin 2012).

Most of the obliquity measurements are available for single hot Jupiters. Some of the smallest planets detected with a Rossiter measurement are GJ 436b ($4.2 \pm 0.2 R_\oplus$), HAT-P-11 b ($4.4 \pm 0.1 R_\oplus$) which are nearly polar (Bourrier et al. 2018; Winn et al. 2010), and 55 Cnc e ($1.94 \pm 0.04 R_\oplus$) which is also misaligned (Bourrier & Hébrard 2014) although the latest result has been put into question (López-Morales et al. 2014). Kepler 408 b is the smallest planet with misaligned orbit among all the planets known to have obliquity measurement (Kamiaka et al. 2019). There are few obliquity detections for multi-planet systems such as KOI-94, Kepler 30 (Hirano et al. 2012; Albrecht et al. 2013; Sanchis-Ojeda et al. 2012) which have coplanar orbits aligned with the stellar rotation.

In this work, we study the multi-planet system hosted by HD3167, which includes two transiting planets and one non-transiting planet. Vanderburg et al. (2016) first reported the presence of two small short-period transiting planets from photometry. The third planet HD3167 d was later discov-

ered from the radial velocity analysis by Christiansen et al. (2017). Gandolfi et al. (2017) found evidence of two additional signals in the RV measurements of HD3167 with periods 6.0 and 10.7 days. However, they could not confirm the nature of these two signals. Furthermore, Christiansen et al. (2017) did not find any signal at 6 or 10.7 days. Masses of the transiting planets were found to be $5.02 \pm 0.38 M_{\oplus}$ for HD3167 b, a hot super-Earth, and $9.80^{+1.30}_{-1.24} M_{\oplus}$ for HD3167 c, a warm sub-Neptune. The non-transiting planet HD3167 d with minimum mass $6.90 \pm 0.71 M_{\oplus}$ orbits the star in 8.51 days. The two transiting planets have orbital periods of 0.96 days and 29.84 days, and radius of $1.70 R_{\oplus}$ and $3.01 R_{\oplus}$, respectively. We measure the sky projected obliquity for HD3167 c whose larger radius makes it the most favorable planet for the obliquity measurements. The long period of planet c compared to planet b also allows us to have three times better sampling of the data during a given transit.

It is difficult to measure the true 3D obliquity and most methods only access the projection of the obliquity. One can measure the sky projected obliquity for a transiting exoplanet by monitoring the star spectrum during planetary transits. During a transit, the partial occultation of the rotating stellar disk gives rise to the asymmetric line profiles which can be detected using different methods such as Rossiter-McLaughlin (RM) anomaly, Doppler Tomography and Reloaded Rossiter-McLaughlin. These methods use different approaches to retrieve the path of the planet across the stellar disk. This allows us to quantify the systematic errors related to the data analysis method. RM anomaly takes into account that asymmetry in line profiles induces an anomaly in the radial velocity of the star (Queloz et al. 2000; Hébrard et al. 2008). However, the changes in the cross-correlation functions (CCFs) morphology are not analyzed. Doppler tomography uses the spectral information present in the CCF of the star rather than just their radial velocity centroids. This method entails tracking the full time-series of spectral CCF, via modeling the additional absorption line profiles superimposed on the star's spectrum, during the planet transit (e.g., Collier Cameron et al. 2010; Bourrier et al. 2015; Crouzet et al. 2017). This model is then subtracted from the CCFs obtained, leaving behind the spectral signature of the light blocked by the planet. Finally, Reloaded Rossiter-McLaughlin is a technique which analyses directly the local CCF occulted by the planet to measure the sky-projected obliquity (e.g., Cegla et al. 2016a; Bourrier et al. 2017). It isolates the CCFs outside and during the transit with no assumptions about the shape of the stellar line profiles.

The amplitude of the RM anomaly is expected to be below 2 ms^{-1} for HD3167 c. Detecting such a low-amplitude effect is challenging, so we decide to check for the robustness and significance of our results using the aforementioned three different methods. The different methods have their respective advantages and limitations. As such, a combined analysis involving the three complementary approaches provides an obliquity measurement which is more robust against systematic effects due to the analysis method.

We measure the sky-projected obliquity of HD3167 c using the above mentioned three methods and finally discuss the dynamics of the system. This paper is structured as follows. We describe the spectroscopic observations during the transit in Section 2. The detection of spectroscopic transit followed by the data analysis using RM anomaly, Doppler

Tomography and Reloaded RM is presented in Section 3. We discuss the obliquity of planets b and d from geometry in Section 4. We study the dynamics of the system in Section 5 and explore the possible outer companion in Section 6. Finally, we conclude in Section 7.

2. Observations

We obtained the spectra of HD3167 during the two transits of planet c on 2016 October 1 and 2017 November 23 with the spectrograph HARPS-N with a total of 35 observations and 24 observations, respectively. HARPS-N, which is located at the 3.58-m Telescopio Nazionale Galileo (TNG, La Palma, Spain), is an echelle spectrograph that allows high-precision radial velocity measurements. Observations were taken with resolving power $R = 115\,000$ with 15 minutes of exposure time. We used the spectrograph with one fiber on the star and the second fiber on a thorium-argon lamp, for observation to have high radial velocity precision. The signal-to-noise ratio (SNR) per pixel at 527 nm for the spectra taken during the 2016 transit was 56 to 117 with an average $\text{SNR} = 87$. The 2017 transit was observed in poor weather conditions with S/N values ranging from 34 to 107 with an average $\text{SNR} = 72$. In this paper, we worked primarily with the 2016 transit data for the reasons explained in Section 3.2.3.

The Data Reduction Software (DRS version 3.7) pipeline was used for extracting the HARPS-N spectra and cross-correlating them with numerical masks following the method described in Baranne et al. (1996) and Pepe et al. (2002). The CCFs obtained were fitted by Gaussians to derive the radial velocities (RVs) and their uncertainties. We tested different numerical masks such as G2, K0, and K5 and also checked the effect of removing some low SNR spectral orders to obtain the CCFs. These tests were performed to improve the dispersion of data after the Keplerian fit. The method of fitting Keplerian is discussed in detail in Section 3.1. Final RVs were obtained from CCFs which were produced using K5 mask and removing the first 15 blue spectral, low-SNR orders.

The resulting RVs with uncertainty are listed in Table 1 for 2016 observations and Table B.1 in appendix B for 2017 observations. The typical uncertainties were between 0.6 and 1.5 ms^{-1} with a mean value of 0.9 ms^{-1} for 2016 data. The stellar and planet parameters for HD3167 system which we used were taken from Table 1 and Table 5 of Christiansen et al. (2017) except the value of limb-darkening coefficient (ϵ) which was taken from Vanderburg et al. (2016).

3. Analysis

3.1. Detection of Spectroscopic transit

Figure 1 displays the radial velocity measurements of HD3167 during the 2016 transit of planet c. The upper panel shows RVs along with the best-fit RM model found from χ^2 minimization (discussed in Section 3.2) and the lower panel shows residual RVs after the fit. The red dashed line is the Keplerian model due to the orbital motion of three planets. During the transit, the deviation between the Keplerian model and the observed RVs is due to the RM anomaly.

Table 1. Radial velocities of HD3167 measured on 2016 October 1 with HARPS-N

BJD	RV (ms ⁻¹)	Uncertainty (ms ⁻¹)
57663.38879	19526.11	0.99
57663.39881	19525.6	0.89
57663.4097	19524.96	0.96
57663.42026	19525.43	0.86
57663.43128	19525.48	0.80
57663.44191	19527.08	0.89
57663.45255	19525.54	0.80
57663.463	19525.72	0.78
57663.47382	19526.8	0.69
57663.48469	19525.99	0.61
57663.49535	19528.41	0.65
57663.5057	19527.32	0.66
57663.51666	19528.51	0.69
57663.52705	19529.29	0.76
57663.53812	19528.75	0.71
57663.54859	19530.09	0.66
57663.5594	19529.57	0.71
57663.56994	19530.79	0.73
57663.58084	19529.89	0.74
57663.59121	19529.66	0.75
57663.60227	19531.37	0.78
57663.61288	19530.97	0.79
57663.62363	19529.69	0.83
57663.63458	19530.74	0.79
57663.64483	19533.16	0.83
57663.65581	19531.99	0.85
57663.66643	19530.85	0.77
57663.67668	19532.44	0.90
57663.68756	19532.86	1.01
57663.69801	19532.29	1.30
57663.70995	19530.61	1.23
57663.7196	19531.13	1.17
57663.73065	19532.3	1.16
57663.74124	19532.95	1.32
57663.75162	19532.51	1.49

To segregate the observation taken during the planet transit, only RVs lying between the beginning of the ingress (T_1) and end of the egress (T_4) were considered. The photometric values of mid-transit (T_0), period (P) and transit duration (T_{14}) of HD3167 c along with their uncertainties were taken from Christiansen et al. (2017). Total uncertainty of ~ 16 min on T_0 , inferred from the respective uncertainties of 15 min, 6 min and 2 min on P , T_1/T_4 and T_0 from Christiansen et al. (2017), was taken into account in determining the RVs outside the transit. Thirteen RVs (8 before + 5 after the transit) were lying outside the transit, while 18 RVs were present inside the transit. Due to uncertainty in the observed T_0 , it was not clear whether the remaining four RVs were present inside or outside the transit. In the following analysis, T_0 is fixed to the photometric value as the uncertainty on T_0 is negligible in our analysis as shown in Section 3.2.2.

The above mentioned 13 RVs outside the transit were not sufficient to find an independent Keplerian model for the three planets. Thus, the orbital parameters for the three planets to fit Keplerian were taken from Table 5 of Chris-

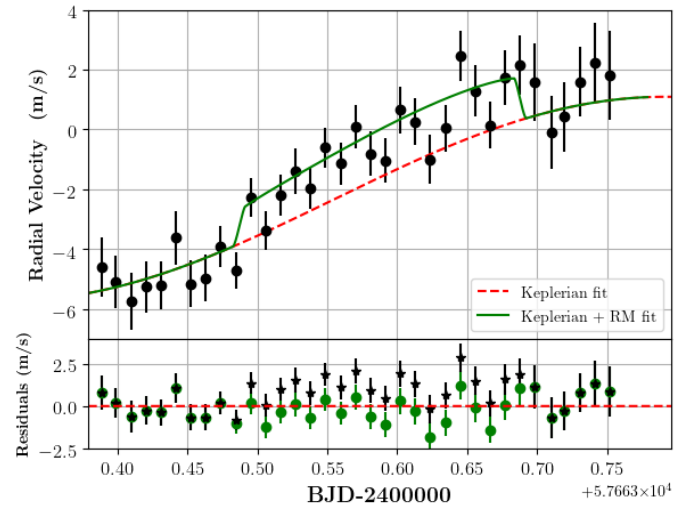


Fig. 1. Radial velocity measurements of HD3167 taken on 2016 October 1 as function of time. *Upper panel:* Solid black circles represent the HARPS-N data, the dashed red line indicates the Keplerian fit while the solid green line depicts the final best-fit with RM effect. *Lower panel:* The black solid circles are the residuals after subtracting the Keplerian and green solid circles are the residuals after subtracting the best-fit RM model.

tiansen et al. (2017) in the equation (1) as

$$RV = \gamma + \sum_{i=1}^3 K_i [\cos(f_i + \omega_i) + e_i \cos \omega_i]. \quad (1)$$

Here K_i represents the radial velocity semi-amplitude, the true anomaly and eccentricity are denoted by f_i and e_i respectively, and ω_i is the argument of periastron. Finally, a Keplerian model was fitted by minimizing the χ^2 considering only one free parameter i.e. the systemic velocity γ . The average of the residual RVs that were taken outside the transit was found to be 0.11 ± 0.72 ms⁻¹, in agreement with the expected uncertainties.

After the Keplerian fit, we noted that the average of residuals RVs inside the transit was 1.17 ± 0.76 ms⁻¹, showing a hint of RM anomaly detection which was fitted using RM model in Section 3.2.2. According to Gaudi & Winn (2007), the expected amplitude of the RM anomaly is 1.7 ms⁻¹ which is within the order of magnitude of the deviation from the Keplerian model observed during the transit.

Furthermore, the slope visible in RVs within the observation time (8.7 hours) was due to the short periodicity of HD3167 b ($P_b = 0.96$ day). To compute the mass of HD3167 b, a Keplerian in the RVs outside the transit was fitted keeping K_b as a free parameter. The K_b was found to be 3.86 ± 0.35 ms⁻¹ corresponding to a planet HD3167 b mass, $M_b = 5.45 \pm 0.50 M_\oplus$. This is consistent with the measurements of Christiansen et al. (2017) ($K_b = 3.58 \pm 0.26$ ms⁻¹, $M_b = 5.02 \pm 0.38 M_\oplus$). K_b was fixed to the more accurate measurement of Christiansen et al. (2017) in further analysis.

We note that the sky-projected obliquity λ was defined as the angle counted positive from the star spin axis toward the orbital plane normal, both projected in the plane of the sky. The sky-projected obliquity was fitted using three different methods, as described in the following sections.

3.2. Rossiter-McLaughlin anomaly

3.2.1. Model

The method developed by Ohta et al. (2005) was implemented to model the shape of the RM anomaly. These authors derived approximate analytic formulae for the anomaly in radial velocity curves, considering the effect of stellar limb darkening. Following their approach, we adopted a model with five free parameters, namely γ , λ , the sky-projected stellar rotational velocity $v \sin i_\star$, the orbital inclination i_p , and the ratio of orbital semi-major axis to stellar radius a/R_\star . The values of radius ratio r_p/R_\star , P , T_0 for HD3167 c were fixed to their photometric values (Christiansen et al. 2017) and ε for HD3167 was fixed to 0.27 (Vanderburg et al. 2016). The parameters i_p and a/R_\star were kept free since their values were poorly constrained from the photometry. Gaussian priors are applied to i_p and a/R_\star as obtained from the photometry (Christiansen et al. 2017). We adopted a value of $v \sin i_\star$ as a Gaussian prior, from the spectroscopy analysis in Christiansen et al. (2017) ($v \sin i_\star = 1.7 \pm 1.1 \text{ km s}^{-1}$). We performed a grid search for the above mentioned free parameters and computed χ^2 at each grid point. The contribution from the uncertainties of i_p , a/R_\star and $v \sin i_\star$ were also added quadratically to χ^2 .

3.2.2. 2016 dataset

The data taken on 2016 October 1 is the best dataset for the obliquity measurement in terms of data quality and sampling of the transit. The 2016 data was fitted with Ohta model and reduced χ^2 with 30 degrees of freedom (n) for the best fit model (RM fit) was found to be 0.95. With the RM fit, the averages of residuals inside and outside the transit were $0.01 \pm 0.75 \text{ ms}^{-1}$, and $0.11 \pm 0.72 \text{ ms}^{-1}$, respectively. The uncertainties obtained were in agreement with the expected uncertainties on the RVs (see column 3 of Table 1). The best-fit value for each parameter corresponds to a minimum of χ^2 . The 1- σ error bars were determined for all five free parameters following the χ^2 variation as described in Hébrard et al. (2002). The best-fit values together with 1 σ error bars are listed in Table 2. We measured $\lambda = -93^\circ_{-15}^{+9}$, indicating a nearly polar orbit.

The derived $v \sin i_\star$ ($2.9_{-1.9}^{+1.4} \text{ km s}^{-1}$) from the RM anomaly suggested to a 2 σ detection of the spectral transit. In order to properly determine the significance of our RM detection, we performed Fischer's classical test. The two models considered for the test were K (only Keplerian) fit and RM (Keplerian+RM) fit. The χ^2 for the K and RM fits are 63.55 (n = 34) and 28.54 (n = 30), respectively. A significant improvement was noted for the second model with $F=2.02$ (p=0.026) obtained using F-test. The improvement to the χ^2 was attributed to the RM anomaly detection with 97% confidence. We concluded that the spectroscopic transit is significantly detected.

As a test, we applied a similar grid procedure without using the spectroscopic constraint on $v \sin i_\star$ from Christiansen et al. (2017). We obtained $\lambda = -91^\circ_{-11}^{+7}$ which is within the 1 σ . The large $v \sin i_\star$ obtained here ($4.8 \pm 2.1 \text{ km s}^{-1}$) did not significantly affect the measurement of λ . Since the planetary orbit was found to be polar and it transits near the center of the star ($b = 0.50 \pm 0.32$, (Christiansen et al. 2017)), the corresponding RM anomaly shape did not put strong constrain on $v \sin i_\star$. The $v \sin i_\star$ can be

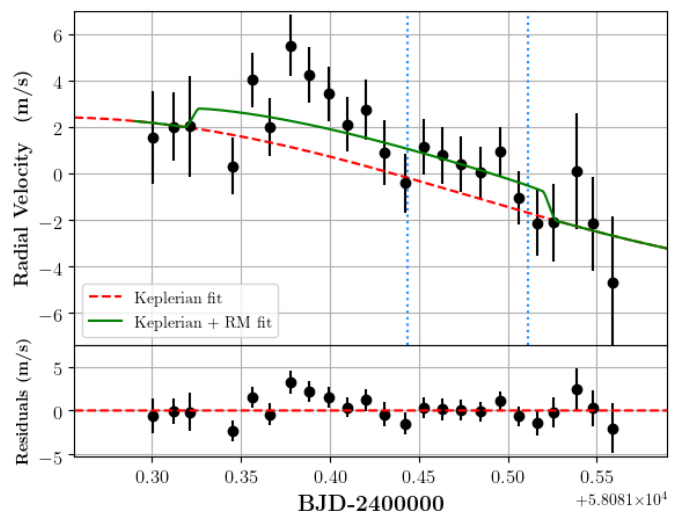


Fig. 2. Radial velocity measurement of HD3167 taken on 2017 November 23 as a function of time. *Upper panel:* Solid black circles represent the HARPS-N data, the dashed red line indicates the Keplerian fit and green line is the over-plotted best-fit RM model from the 2016 transit. The blue dotted line marks the ingress and egress of planet b transit. The expected RM amplitude due to planet b transit is 0.6 ms^{-1} . *Lower panel:* The residuals after subtracting the best-fit RM.

estimated more accurately using Doppler tomography technique in Section 3.3.

Furthermore, the effect of fixed parameters such as r_p/R_\star , P , T_0 , T_{14} and K_b on λ was investigated. When these fixed parameters were varied within their 1 σ uncertainty, λ was found to remain within the 1 σ uncertainty derived above.

3.2.3. 2017 dataset

Here, we evaluated whether or not the lower-quality 2017 dataset agrees with the results obtained above using the 2016 dataset. We first determined the observations taken outside the 2017 transit using the same method as explained in Section 3.1. After considering uncertainty on T_0 , we found only one RV measurement which was taken clearly outside the transit. The scarcity of data and poor data sampling outside the transit and along with the low-quality observations during 2017 transit hindered us to find a good model for Keplerian and finally an independent value of λ . Thus the RM model parameters were fixed to the best-fit values from the 2016 transit and the model derived previously was scaled to the RV level of this epoch. We also noted that during the 2017 transit, HD3167 b and HD3167 c are transiting simultaneously. However, the expected amplitude of the RM anomaly from HD3167 b is 0.56 ms^{-1} which is small compared to the RM signal from HD3167 c and the RV measurements accuracy.

Figure 2 shows the best-fit RM model from 3.2.2, during the 2017 transit and the residuals after subtracting the best-fit RM. This fit showed that the 2017 dataset roughly agreed with the results obtained from the RM anomaly fitted in 2016 observations; despite its lower quality, it did not infrim the results presented above in Section 3.2.2. The average of residuals inside and outside the transit was found to be $0.22 \pm 1.29 \text{ ms}^{-1}$, and $0.39 \pm 1.66 \text{ ms}^{-1}$, respectively.

The obtained uncertainties were slightly larger than the expected uncertainties on the RVs. The 2017 dataset presented short-term variations in the first half of the transit which could not be due to RM or Keplerian effects. We interpreted them as an artifact due to the bad weather conditions. Since there was no significant improvement from fitting RM anomaly ($F=1.73$, $p=0.10$), we considered the spectroscopic transit was not significantly detected in the 2017 data. Thus, the 2017 dataset was not considered for further analysis.

3.3. Doppler Tomography

Here we present the obliquity measurement we performed on the 2016 dataset using Doppler tomography in order to compare it with the measurement from RM anomaly technique presented above. When a planet transits its host star, it blocks different regions of the rotating stellar disk, which induces a Gaussian bump to the spectral lines of the star. This bump can be tracked by inspecting the changes in the CCF which allows us to measure the obliquity. It can also obtain an estimate of the stellar rotational speed independent from the spectroscopic estimate by Christiansen et al. (2017). The CCFs obtained from the DRS with the K5 mask were used for this analysis (Section 2). Following the approach of Collier Cameron et al. (2010), a model of stellar CCF, which is the convolution of limb-darkened rotation profile with a Gaussian corresponding to the intrinsic photospheric line profile and instrumental broadening, was considered. When the CCFs are fitted by the model including the stellar spectrum and the transit signature, some residual fixed patterns appear that are constant all over the full night. These patterns, also called “sidelobes” by Collier Cameron et al. (2010), are produced by coincidental random alignments between some stellar lines and the lines in the mask when the mask is shifted to calculate the CCFs. To remove these patterns we assume that they do not vary within the night and we average the residuals of the out-of-transit CCFs after subtracting the best fit to the CCFs calculated by considering the stellar spectrum only. We made a tomographic model which depends on the same parameters as the Keplerian + RM model (Sect. 3.2), with the addition of the local line profile width, s (non rotating local CCF width) expressed in units of the projected stellar rotational velocity (Collier Cameron et al. 2010). The most critical free parameters used for fitting the aforementioned Gaussian bump were λ , $v \sin i_\star$, γ , i_p , a/R_\star and s . Other parameters such as P , r_p/R_\star , T_0 and ε were fixed to the same values used for RM fit.

The following merit function was used to fit the CCFs as done in Bourrier et al. (2015):

$$\chi^2 = \sum_i^{n_{ccf}} \sum_j^{n_u} \left[\frac{f_{i,j}(\text{model}) - f_{i,j}(\text{obs})}{\sigma_i} \right]^2 + \sum_{a_p/R_\star, i_p} \left[\frac{x_{\text{tomo}} - x_{\text{photo}}}{\sigma_{x_{\text{photo}}}} \right]^2,$$

where $f_{i,j}$ is the flux at velocity point j in the i_{th} observed or model CCFs. The error on the CCF estimate is supposed to be constant over the full velocity range for a given CCF. To find the errors σ_i on the CCF profiles, we first used the constant errors which are the dispersion of the residuals between the CCFs and the best-fit model profiles. As the CCFs were obtained using DRS pipeline with a velocity resolution of 0.25 km s^{-1} and the spectra has a reso-

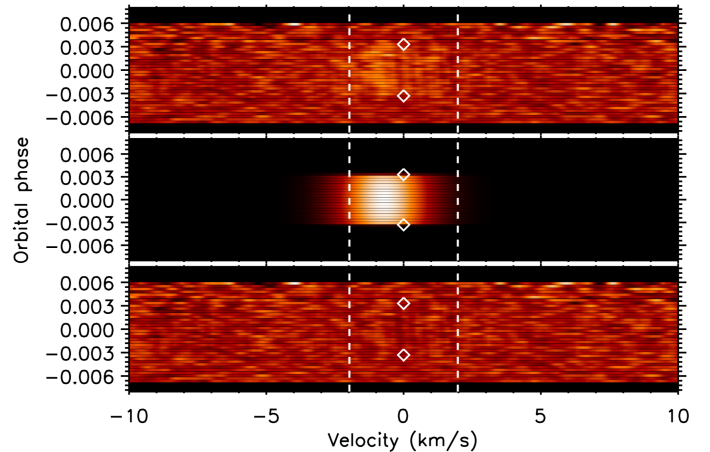


Fig. 3. Maps of the time-series CCFs as a function of radial velocity relative to the star (in abscissa) and orbital phase (in ordinate). The dashed vertical white lines are marked at $\pm v \sin i_\star$, and 1st and 4th contacts of transit are indicated by white diamonds. *Upper panel:* Map of the transit residuals after subtracting the model stellar profile. The signature of HD3167 c is the moderately bright feature visible from ingress to egress. *Middle panel:* The transiting signature of HD3167 c using best-fit model, obtained with $\lambda = -90^\circ$. *Lower panel:* Overall residual map after subtracting the model planet signature.

lution of 7.5 km s^{-1} , the residuals were found to be strongly correlated. This led to the underestimation of error bars on the derived parameters. A similar analysis as in Bourrier et al. (2015) was used to retrieve the non-correlated Gaussian component of the CCFs. The residuals variance as a function of data binning size (n_{bin}) is well represented by a quadratic harmonic combination of a white and red noise component:

$$\sigma^2(n_{bin}) = \left(\left(\frac{n_{bin}}{\sigma_{Uncorr}^2} \right)^2 + \left(\frac{1}{\sigma_{Corr}^2} \right)^2 \right)^{-\frac{1}{2}}$$

where $\sigma_{Uncorr}/\sqrt{n_{bin}}$ is the intrinsic uncorrelated noise and σ_{Corr} is the constant term characterizing the correlation between the binned pixels. We adopted gaussian priors for the i_p and a/R_\star from the photometry (Christiansen et al. 2017).

The transit of the planet was clearly detected from the CCF profiles as shown in the Figure 3. The $v \sin i_\star$ was found to be $2.1 \pm 0.5 \text{ ms}^{-1}$ which is consistent with the estimate from spectroscopy ($v \sin i_\star = 1.7 \pm 1.1 \text{ km s}^{-1}$). The sky projected obliquity was measured to be $\lambda = -90^\circ \pm 14^\circ$ which is in accordance with the result from the RM analysis (see Section 3.2.2). Table 2 lists the best-fit values together with 1σ error bars.

We also performed a test to check the effect of the fixed parameter T_0 by varying within 1σ error bars. The value of λ remained within the 1σ uncertainty derived above.

3.4. Reloaded Rossiter-McLaughlin technique

We applied the reloaded RM technique (Cegla et al. 2016a; Bourrier et al. 2018) to the HARPS-N observations of HD3167 c. CCFs computed with the K5 mask (Section 2) were first corrected for the Keplerian motion of the star induced by the three planets in the system (calculated

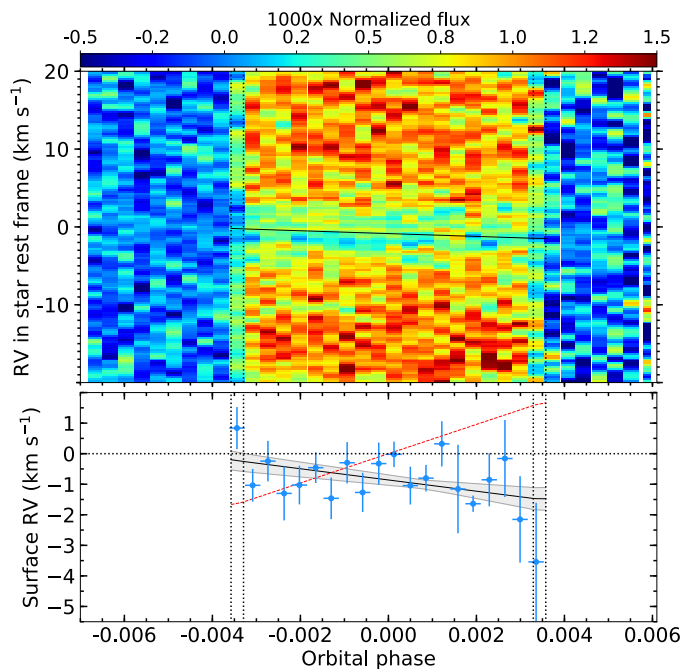


Fig. 4. *Upper panel:* Map of the residual CCF series, as a function of orbital phase (in abscissa) and radial velocity in the stellar rest frame (in ordinate). Colors indicate flux values. The four vertical dashed black lines show the times of transit contacts. The in-transit residual CCFs correspond to the average stellar line profiles from the regions occulted by HD 3167 c across the stellar disk. The solid black line is the best-fit model to the local RVs of the planet-occulted regions ($\lambda = -112.5^\circ$), assuming solid-body rotation for the star ($v \sin i_\star = 1.89 \text{ km s}^{-1}$). *Lower panel:* RVs of the stellar surface regions occulted by the planet (blue points), best-fitted with the solid black line (same as in the upper panel). The grey area corresponds to the 1σ envelope of the best-fit, derived from the MCMC posterior distributions. The dashed red line shows a model obtained with the same stellar rotational velocity but an aligned orbit ($\lambda = 0^\circ$), highlighting the large orbital misalignment of HD 3167 c.

with the properties from Christiansen et al. (2017)). The CCFs outside of the transit were co-added to build a master-out CCF, whose continuum was normalized to unity. The centroid of the master out CCF, derived with a Gaussian fit, was used to align the CCFs in the star rest frame. The continuum of all CCFs was then scaled to reflect the planetary disk absorption by HD 3167 c, using a light curve computed with the *batman* package (Kreidberg 2015) and the properties from Christiansen et al. (2017). Residual CCFs were obtained by subtracting the scaled CCF from the master-out (Figure 4).

No spurious features are observed in the residual CCFs out of the transit. Within the transit, the residual RM spectrally and spatially resolve the photosphere of the star along the transit chord. The average stellar lines from the planet-occulted regions are clearly detected and were fitted with independent Gaussian profiles to derive the local RVs of the stellar surface. We used Levenberg-Marquardt least-squares minimization, setting flux errors on the residual CCFs to the standard deviation in their continuum flux. Since the CCFs are oversampled in radial velocity, we kept one in four points to perform the fit. All average local stellar lines were well fitted with Gaussian profiles, and their contrast

was detected at more than 3σ (using the criterion defined by Allart et al. (2017)). The local RV series was fitted with the model described in Cegla et al. (2016a) and Bourrier et al. (2017), assuming solid-body rotation for the star. We sampled the posterior distributions of $v \sin i_\star$ and λ using the Markov chain Monte Carlo (MCMC) software *emcee* (Foreman-Mackey et al. 2013), assuming uniform priors. Best-fit values were set to the medians of the distributions, with 1σ uncertainties derived by taking limits at 34.15% on either side of the median. The best-fit model shown in Fig 4 corresponds to $v \sin i_\star = 1.9 \pm 0.3 \text{ km s}^{-1}$ and $\lambda = -112.5^{+8.7}_{-8.5}$, which agree at better than 1.4σ with the results obtained from the RM and Doppler Tomography (Section 3.2 and 3.3). The error bars on λ are small because i_p and a/R_\star were fixed in this particular analysis. However, when i_p , T_0 , and a/R_\star were varied within their 1σ uncertainty, λ did not vary significantly and remained within 1σ uncertainty. The best-fit values with their 1σ uncertainties are listed in Table 2.

3.5. Comparison between the three methods

The most commonly used method to estimate sky-projected obliquity using RV measurements is the analysis of the RM anomaly. However, RM method does not exploit the full spectral CCF. In some extreme cases, the classical RM method can introduce large biases in the sky-projected obliquity because of asymmetries in the local stellar line profile or variations in its shape across the transit chord (Cegla et al. 2016b). The Doppler tomography method is less affected compared to the RM anomaly method, as it explores the full information in the CCF. However, the assumption of a constant, symmetric line profile, and ignoring the effects of the differential rotation, can also introduce bias in the obliquity measurements. Results from the reloaded RM technique suggest that the bias is not significant here. The Reloaded RM technique does not make prior assumptions of the local stellar line profiles and allows a clean and direct extraction of the stellar surface RVs along the transit chord. This results in an improved precision on the obliquity, albeit under the assumption that the transit light curve parameters (in particular the impact parameter and planet-to-star radius ratio) are known to a good enough precision to be fixed. In the present case, we might thus be underestimating the uncertainties on λ with this method.

The sky-projected obliquities measured by all three methods agree at better than 1.4σ . This confirms the detection of the spectroscopic transit in the 2016 data is significant and suggests the corresponding obliquity measurement is not reached by strong systematics due to the method. Combining the λ values from all three methods, we estimated the sky-projected obliquity for HD 3167 c to be $\lambda = -98^\circ \pm 23^\circ$, after taking into account both the systematic and statistical errors. We adopted that conservative value on our final obliquity measurement.

As discussed in Section 3.2.2, stellar rotation speed was not well constrained by the RM method. However, $v \sin i_\star$ more accurately measured from Doppler Tomography and Reloaded RM technique was consistent with the measurements of Christiansen et al. (2017). The $v \sin i_\star$ from three methods were also found to be within 1σ . Furthermore, the two photometric parameters a/R_\star and i_p were also in agree-

Table 2. Best fit Parameters using three methods

Parameter(Unit)	RM fit	Doppler Tomography	Reloaded RM	Previously Published Values
λ (degrees)	-93.0^{+9}_{-15}	-90 ± 14	$-112.5^{+8.7}_{-8.5}$	-
$v \sin i_{\star}$ (kms $^{-1}$)	$2.9^{+1.4}_{-1.8}$	2.1 ± 0.4	1.9 ± 0.3	1.7 ± 1.1 (1)
γ (kms $^{-1}$)	$19.5310^{+0.0003}_{-0.0002}$	19.5270 ± 0.0080	19.5286 ± 0.0062	-
i_p (degrees)	$89.5^{+0.3}_{-1.1}$	$88.94^{+0.5}_{-0.4}$	89.3^{\star}	$89.3^{+0.5}_{-0.96}$ (1)
a/R_{\star}	$43.3^{+3.3}_{-13.8}$	36^{+12}_{-6}	40.323^{\star}	$40.323^{+5.55}_{-12.62}$ (1)

★: Fixed to their photometric value (Christiansen et al. 2017)

References. (1) Christiansen et al. (2017)

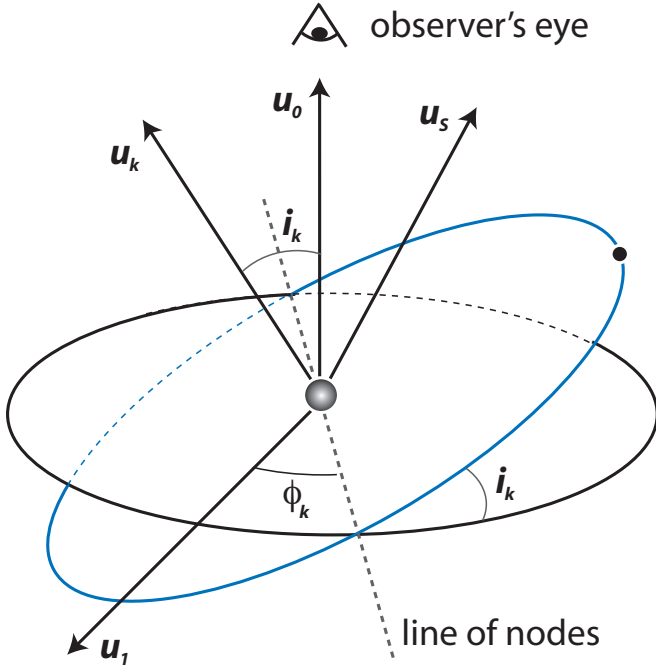


Fig. 5. Pictorial representation of the reference angles and the unit vectors. \mathbf{u}_s corresponds to the direction of the star's spin.

ment within their uncertainties for the RM and Doppler Tomography methods. The systemic velocity γ is slightly different in each case due to the different definition employed in each method.

4. Obliquity of planets b and d from geometry

The spectroscopic transit observations gave constraints only on the obliquity of the planet c. Although the planet b is also transiting, the low amplitude for the RM signal during the transit precludes us for measuring its obliquity with the present data. However, because both planets b and c are transiting planets, the mutual inclination can be constrained.

We denoted by \mathbf{u}_0 the unit vector along the line of sight directed towards the Earth and \mathbf{u}_1 a unit vector perpendicular to \mathbf{u}_0 , that is in the plane of the sky (see Figure 5). The orbital planes of the planets b and c were characterized by the perpendicular unit vectors \mathbf{u}_b and \mathbf{u}_c . The inclination of their orbits, i_b and i_c , have been constrained to be $i_b = 83.4^{+4.6}_{-7.7}$, and $i_c = 89.3^{+0.5}_{-0.96}$ (Christiansen et al. 2017). For a planet k (here k stands for either b or d), we defined ϕ_k as the angle between \mathbf{u}_1 and the projection of \mathbf{u}_k on the plane of the sky (this is equivalent to the longitude of the ascending node in the plane of the sky). With these definitions, the mutual inclination between the planets b and c, i_{bc} , is given by :

$$\cos i_{bc} = \cos i_b \cos i_c + \sin i_b \sin i_c \cos(\phi_b - \phi_c) \quad (2)$$

With $\cos i_b$ and $\cos i_c$ uniformly distributed within their 1σ error bars and assuming that ϕ_b and ϕ_c are uniformly distributed between 0 and 2π , we calculated the probability distribution of i_{bc} (Fig. 6). The probability distribution was found to be close to a uniform distribution, except it is low for i_{bc} below 10° and above 170° . So from geometry, no information on the planet b obliquity could be derived from our measurement of the planet c obliquity. We noted that in the case of two non-transiting planets, the probability distribution of i_{bc} would be peaked around 90° as shown by the dotted line in Figure 6.

Planet d would transit if the condition

$$i_{dc} \leq \arctan\left(\frac{R_{\star}}{a_d}\right) - (90 - i_c) \quad (3)$$

is fulfilled, where R_{\star} is the star radius and a_d is planet d semi-major axis. Since, the planet d is not transiting, the mutual inclination between planets c and d must be at least 2.3° .

As a result, the obliquity of planets b and d cannot be constrained well just from the geometry of the planetary system. We put constrain on the obliquity of planet d from the dynamics of the planetary system in Section 5.

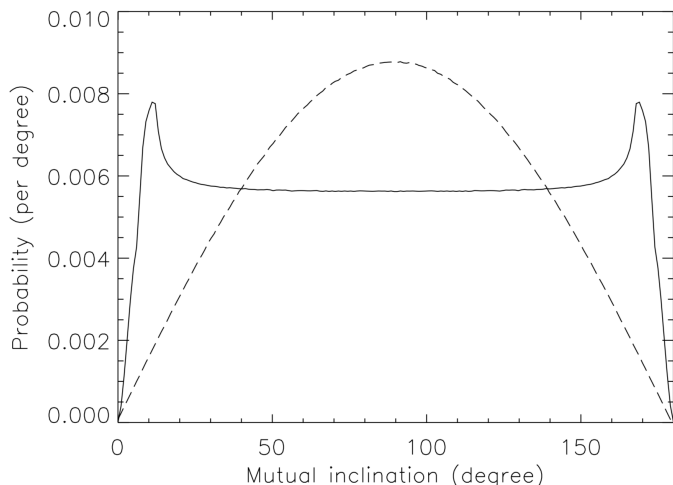


Fig. 6. The probability distribution of the mutual inclination between the planets b and c (solid line). For comparison, the dotted line shows the probability distribution in the case where both planets are non-transiting.

5. Dynamics

5.1. Planet mutual inclinations

While the available observations were unable to geometrically constrain the planets mutual inclinations, a bound is given by the stability analysis of the system.

Short-period planets with aligned orbit such as KELT-24 b, WASP-152 b (Rodriguez et al. 2019; Santerne et al. 2016) or misaligned orbit such as Kepler-408 b, GJ436 b (Kamiaka et al. 2019; Bourrier et al. 2018) have been detected. The obliquity distribution of short-period planets is not clear. However, since planet b is close to the star, its orbit is most likely circular and its inclination is governed by the interaction with the star as shown in appendix A.2. The exact inclination of planet b is not important from a

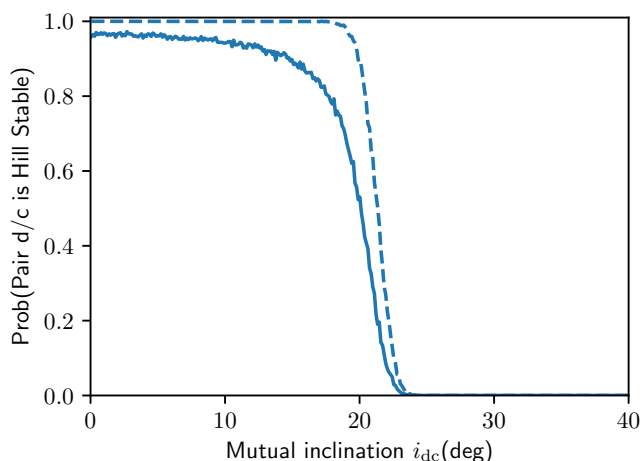


Fig. 7. Probability of the pair d/c to be Hill stable as a function of the mutual inclination of d and c assuming planet b is within the invariant plane. The masses, semi-major axes, and eccentricity are drawn from the best-fit distribution (Christiansen et al. 2017). The dashed curve corresponds to a system where every planet is on a circular orbit.

dynamical point of view and it is safe to neglect planet b's influence when investigating the stability of the system. We focus here on the outer pair of planets to constrain the system and study the simplified system only composed of the star and the two outer planets. Our goal is to determine the maximum mutual inclination between planets d and c such that the outer pair remains Hill stable (Petit et al. 2018; Marchal & Bozis 1982). We first create 10^6 realizations of HD3167 system by drawing from the masses, eccentricities and semi-major axes distributions given by Christiansen et al. (2017) best fit. To each of those copies of the system, we set the mutual inclination between planets c and d with values uniformly spaced between 0° and 90° .

We assume that planet b's orbit is in the invariant plane, i.e. the plane perpendicular to the angular momentum vector of the whole system¹. As a result we can compute the inclinations i_c and i_d with respect to the invariant plane since the projection of the angular momentum on the invariant plane gives

$$G_c \sin(i_c) = G_d \sin(i_d), \quad (4)$$

where $G_k = m_k \sqrt{GM_s a_k (1 - e_k^2)}$ is the norm of the angular momentum of planet k . Then, we compute the total angular momentum deficit (AMD, Laskar 1997) of the system

$$C = \sum_{k=b,c,d} m_k \sqrt{GM_s a_k} \left(1 - \sqrt{1 - e_k^2} \cos(i_k) \right), \quad (5)$$

and we determine whether the pair d/c is Hill stable or not. To do so, we compare the AMD to the Hill critical AMD of the pair (eq. 30, Petit et al. 2018). We plot on Figure 7 the proportion of Hill stable system binned by mutual inclination i_{dc} . We also plot the proportion of Hill stable pair for a system with circular orbit.

We observe that for an inclination i_{dc} below 21° , the system is almost certainly Hill stable. It means that for any orbital configuration and masses compatible with the observational constraints, the system will be long-lived with such a low mutual inclination. We emphasize that long-lived configurations with higher mutual inclination than 21° exist. Christiansen et al. (2017) give the example of Kozai-Lidov oscillations with initial mutual inclinations up to 65° . However, the choice of initial conditions is fine tuned because of the circular orbits (a configuration that is rather unlikely for such dynamically excited systems).

If we assume that the star spin is aligned with the total angular momentum of the planets, the planet obliquity corresponds to the planet inclination with respect to the invariant plane. Assuming $i_{dc} < 21^\circ$, the maximum obliquity of planet c is about 9° . Even if the mutual inclination $i_{dc} = 65^\circ$, the obliquity only reaches 32° . Thus, the observed polar orbit shows that the star spin cannot be aligned with the planet angular momentum.

From Section 4 and the previous paragraphs, we deduce that the most likely value for i_{dc} is between 2.3° and 21° . Since the mutual inclination of planets c and d is low, we can conclude that planet d is also nearly polar.

¹ We make the assumption that planet b is within the invariant plane in order to be able to compute the AMD as a function of the mutual inclination i_{dc} . Nevertheless the actual inclination has little influence on the stability of the pair d/c.

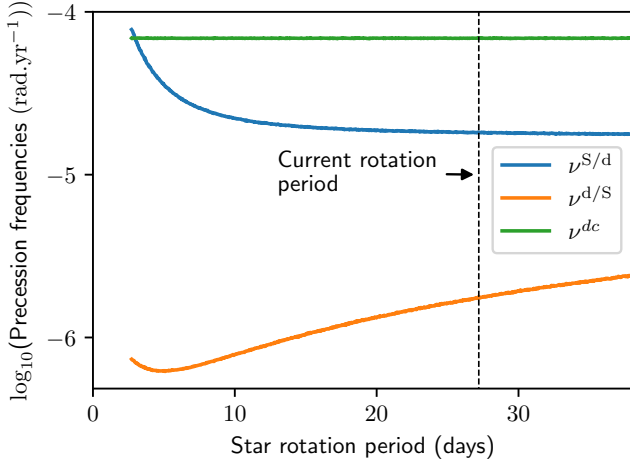


Fig. 8. Characteristic frequencies defined in Eq. (A.5) as a function of the star period. The current star estimated rotation period is marked with a vertical dashed line. The two terms $\nu^{d/c}$ and $\nu^{c/d}$ are merged into a single curve ν^{dc} , because they are almost equal.

5.2. Planets-stellar spin interactions

Since the system’s eccentricities and mutual inclinations are most likely low to moderate, we consider the interaction between the stellar spin and the planetary system. In particular, we investigate if the motion of the planets can effectively tilt the star up to an inclination that could explain the polar orbit of planets c and d. As of today, Christiansen et al. (2017) estimate the star rotation period to 27.2 ± 7 days but it may have slowed down by a factor 10 (Bouvier 2013). In order to investigate the evolution of the obliquity that could have happened in earlier stages of the system life, we study the planet-star interaction as a function of the star rotation period.

To do so, we apply the framework of the integrable 3-vectors problem to the star and the angular momenta of planets d and c (Boué & Laskar 2006; Boué & Fabrycky 2014; Correia 2015). This model gives both the qualitative and quantitative behavior of the evolution of three vectors representing different angular momenta directions \mathbf{u}_S , \mathbf{u}_d and \mathbf{u}_c under their mutual interactions. We detail the model in appendix A.

As shown in Boué & Fabrycky (2014), the mutual interactions of the three vectors can be described by comparing the different characteristic frequencies² of the system $\nu^{d/S}$, $\nu^{S/d}$, $\nu^{d/c}$ and $\nu^{c/d}$ of expressions given in (A.5). The frequency $\nu^{j/k}$ represents the relative influence of the body j over the motion of \mathbf{u}_k . In other words, if $\nu^{k/j} \ll \nu^{j/k}$, \mathbf{u}_j is almost constant while \mathbf{u}_k precesses around. In this study, we neglect the interactions between the star and planet c versus the one between the star and planet d because they are smaller by two orders of magnitude.

Due to its coupling with the star, planet b acts as a bulge on the star that enhances the coupling between the outer planet orbits and the star (see appendix A.2). We limit our

study to the configuration where the strongest coupling occurs i.e. when planet b’s orbit lies within the star equatorial plane. Planet b’s influence modifies the characteristic frequencies $\nu^{d/S}$ and $\nu^{S/d}$ as it is shown in appendix A.2. The model is valid in the secular approximation if planets d and c eccentricities remain small such that G_d and G_c are constant. Boué & Laskar (2006) showed that the motion is quasiperiodic. It is possible to give the maximum spin-orbit angle of planet c as a function of the initial inclination of planet d.

Using the classification of (Boué & Fabrycky 2014, section 5.3.), we can determine the maximum misalignment between \mathbf{u}_S and \mathbf{u}_c as a function of the initial inclination between \mathbf{u}_S and \mathbf{u}_d . We plot the frequencies (cf. Eq. (A.5)) as a function of the star rotation period on Figure 8. We merged the curves representing $\nu^{d/c}$ and $\nu^{c/d}$ into ν^{dc} because the two terms are almost equal.

We are in a regime where $(\nu^{d/c} \sim \nu^{c/d}) \gg (\nu^{d/S}, \nu^{S/d})$ with the orbital frequencies dominating the interactions with the star. For the shorter periods we have $(\nu^{d/c} \sim \nu^{c/d} \sim \nu^{S/d}) \gg \nu^{d/S}$. But nonetheless, in both cases the dynamics are purely orbital, i.e. the star acts as a point mass and is never coupled with the outer planet orbits. It is not possible for the planets c and d to reach a large mutual inclination with the star spin axis starting from almost coplanar orbits or even moderate inclination. In the case of misalignment of planet b with the star, it will be even harder for the planets to tilt the star.

We conclude that even if the star had a shorter period in the past, it is unlikely that the currently observed system can, by itself, generates such a large obliquity for planet c and d. However, large initial obliquities are almost conserved, which means that the observed polar orbits are possible under the assumptions made, while not explained by this scenario.

5.3. System tilt due to an unseen companion

We now assume that, while the system only presents moderate inclinations, there exists a distant companion on an inclined orbit. We look at the configurations that can lead to tilting the system with respect to the star. Once again, we use the framework of Boué & Fabrycky (2014). We consider the vectors \mathbf{u}_S , \mathbf{u} and \mathbf{u}' that respectively give the direction of the star spin axis \mathbf{S} , the total angular momentum of the planetary system \mathbf{G} and the angular momentum of the companion \mathbf{G}' . The outer companion is described by its mass m' , its semi-major axis a' , its semi-minor axis $b' = a' \sqrt{1 - e'^2}$ and its initial inclination I_0 with respect to the rest of the system assumed nearly coplanar or with moderate inclinations. Moreover, we assume that \mathbf{G} is initially aligned with \mathbf{S} while the companion inclination is large with respect to the planetary system, i.e. I_0 is larger than 45° up to 90° . According to Boué & Fabrycky (2014), all interactions between planets cancel out because we only consider the dynamics of their total angular momentum \mathbf{G} .

As in the previous part, we can compare the different characteristics frequencies of the system $\nu^{pla/S}$, $\nu^{S/pla}$, $\nu^{comp/pla}$ and $\nu^{pla/comp}$ of expression given in Eqs. (A.6) and (A.7). The companion effectively tilts the planetary system as a single body if its influence on planet c is small with respect to the interaction between planets d and c. In the other case, planet c will enter Lidov-Kozai oscillations which can lead

² The characteristics frequencies designate the coupling parameters between the different vector considered as explained in appendix A. They have the dimension of a frequency but are not properly speaking the frequencies of the system. Here, we use the terminology introduced in Boué & Fabrycky (2014).

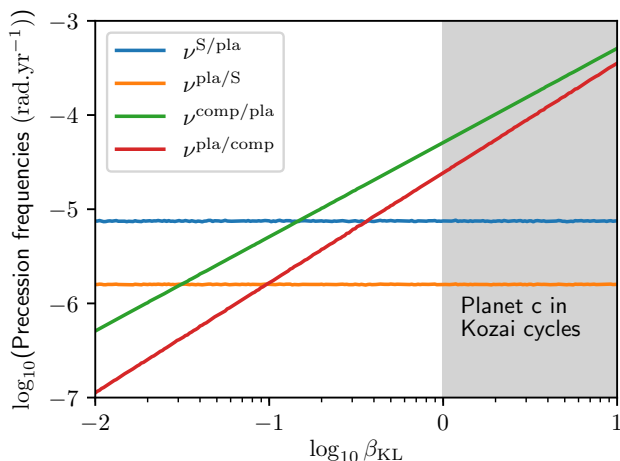


Fig. 9. Characteristic frequencies defined in Eq. (A.6) as a function of β_{KL} (see Eq. 6). For $\beta_{\text{KL}} > 1$, the outer companion can destabilize the observed system.

to the destabilization of the system due to the interactions with planet d. Boué & Fabrycky (2014) give the limit where the outer companion starts to perturb the planetary system and excites the outer planet through Kozai-Lidov cycles. Indeed, they explain that if the coefficient β_{KL} defined as

$$\beta_{\text{KL}} = \frac{m'}{m_d} \left(\frac{a_c}{a_d} \right)^2 \left(\frac{a_c}{b'} \right)^3, \quad (6)$$

verifies $\beta_{\text{KL}} \ll 1$, the companion's influence does not perturb the system and tilts it as a whole.

We plot on Figure 9 the frequencies $\nu^{\text{pla}/S}$, $\nu^{S/\text{pla}}$, $\nu^{\text{comp}/\text{pla}}$ and $\nu^{\text{pla}/\text{comp}}$ as a function of β_{KL} and we observe different regimes. In the first one, we have $\beta_{\text{KL}} < 0.1$ and $\nu^{\text{pla}/\text{comp}} \ll \nu^{\text{comp}/\text{pla}} \ll \nu^{S/\text{pla}}$. The influence of the companion is too small to change the obliquity of the planetary system. For $\beta_{\text{KL}} > 1$, we have $(\nu^{\text{pla}/\text{comp}} \sim \nu^{\text{comp}/\text{pla}}) \gg \nu^{S/\text{pla}}$ which is a regime where the system obliquity can reach I_0 . However, the companion destabilizes the orbit of planet c which can lead to an increase of eccentricity and mutual inclination between the planets. For $0.1 \lesssim \beta_{\text{KL}} \lesssim 1$, we remark that $\nu^{\text{pla}/S} \ll (\nu^{\text{pla}/\text{comp}} \sim \nu^{\text{comp}/\text{pla}} \sim \nu^{S/\text{pla}})$. According to Boué & Fabrycky's classification, the maximum possible inclination between the star and the planet *i.e.* their obliquity is almost twice I_0 for $I_0 \lesssim 80^\circ$. In this regime, an unseen companion can explain the observed polar orbits of HD3167 c and d.

We conclude that some stable configurations with an additional, outer companion may explain the high obliquity of planets c and d. We further discuss the possible presence of outer companion signals in the existing radial velocity data in Section 6. Accurate measurement of planets d and c eccentricities will also help to constrain more such a scenario.

6. Outer Companion

To find the possible signatures of an outer companion, we performed two different tests on the radial velocity data from Christiansen et al. (2017), which cover a span of five months. Firstly we obtained the residual radial velocity after removing the Keplerian signal due to the 3 planets. In the analysis performed by Christiansen et al. (2017), the

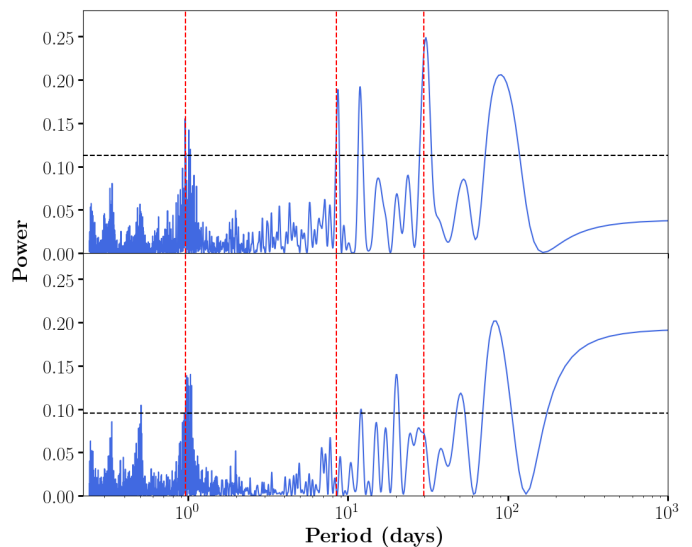


Fig. 10. *Upper Panel:* Lomb-Scargle Periodogram of the RV of HD3167 taken from Christiansen et al. (2017). Black dashed line represents the False Alarm Probability at 0.1% and three vertical red dashed lines corresponds to the period of the 3 planets already detected around HD3167. *Lower Panel:* Lomb-Scargle Periodogram of the RV data after removal of the three known periodic signals.

linear drift was fixed to $0 \text{ ms}^{-1}\text{yr}^{-1}$ before fitting the Keplerian. However, we detected a linear drift of $7.6 \pm 1.6 \text{ ms}^{-1}\text{yr}^{-1}$ in the residual velocities. Assuming a circular orbit for the outer companion, this linear drift corresponds to a minimum period of 350 days and a minimum mass of $0.1 M_{\text{Jup}}$. Such a body have a $\beta_{\text{KL}} \approx 0.08$, which makes it unlikely to be able to incline the planets c and d with respect to the star.

Secondly, we generated the periodogram of the radial velocity before and after the removal of three known periodic signal using Lomb-Scargle method as shown in Figure 10. Apart from the detected planets, two other peaks at 11 days and 78 days were found to be above 0.1% False Alarm Probability (FAP) in the Fourier power. The peak at 11 days was an alias caused by the sampling being concentrated around lunar cycles as explained in Christiansen et al. (2017). In the lower panel of Figure 10, there was no peak at 11 days, but the peak at 78 days was persistent in both periodograms. The peak around 20 days in the lower panel may be caused by stellar rotation and peak around 1 day was an alias due to data sampling. Assuming a circular orbit of 78 days period, it corresponds to a minimum mass of $0.03 M_{\text{Jup}}$ for the outer companion, which gives $\beta_{\text{KL}} \approx 0.5$. This potential outer companion might explain the high obliquity of HD3167 c if its initial inclination I_0 was large enough.

We found possible indications of an additional, outer companion in the system. Extra RV observations of HD3167 on a long time span are necessary to conclusively establish its presence and determine its orbital characteristics, and thus confirm our hypothesis.

7. Conclusion

We use new observations obtained with HARPS-N to measure the obliquity of a sub-Neptune in a multi-planetary

system. The three different methods we applied on this challenging dataset agree, making robust the sky-projected obliquity we measured. We report a nearly polar orbit for the HD3167 c with $\lambda \sim -98^\circ \pm 23^\circ$. The measurements of λ from RM anomaly, Doppler Tomography and Reloaded RM technique agree at better than 1.4σ standard deviation with this value. The $v \sin i_\star$ from three methods is also in agreement within their uncertainties. To our knowledge, this is the first time these three methods are applied and compared to the spectroscopic observation of a planetary transit.

These observations bring a valuable addition to the known planetary obliquity sample, extending it further beyond hot Jupiters. Several small-radius multi-planet systems with aligned spin-orbit such as Kepler 30 (Sanchis-Ojeda et al. 2012) and misaligned spin-orbit such as Kepler 56 (Huber et al. 2013) have been reported. Additionally, single, small exoplanets with high obliquity measurement such as Kepler 408 (Kamiaka et al. 2019) and GJ436 (Bourrier et al. 2018) have also been reported. Some of the misalignments can be possibly explained by the presence of an outer companion in the system. One particularly interesting planetary system is Kepler 56 with two of its transiting planets misaligned with respect to the rotation axis of their host star. This misalignment was explained by the presence of a massive, non-transiting companion in the system (Huber et al. 2013). A third planet in the Kepler-56 system was later discovered by Otor et al. (2016) which supported the finding of Huber et al. (2013). Similarly, HAT-P-11 b misalignment may be explained by the presence of HAT-P-11 c (Yee et al. 2018).

Our dynamical analysis of the system HD3167 put constraints on the obliquities of planet d. We can not determine the obliquity of planet b with the current data and information about the system. The Hill stability criterion shows that the orbits of planets c and d are nearly coplanar so that both planets are in nearly polar orbits. The planet-stellar spin interactions cannot provide a satisfactory explanation for the polar orbits of planets c and d. We postulate that there might exist an additional, unseen companion in the system which could explain the polar orbits of planets c and d. Hints for additional, outer companions are present in the available RV dataset. Continued radial velocity measurements of HD3167 on a longer time span might reveal the outer companion and confirm our speculation.

Acknowledgements. A. P. thanks G. Boué for the helpful discussions during the study. A.C. acknowledges support from CFISUC strategic project (UID/FIS/04564/2019), ENGAGE SKA (POCI-01-0145-FEDER-022217), and PHOBOS (POCI-01-0145-FEDER-029932), funded by COMPETE 2020 and FCT, Portugal. V. B. acknowledges support by the Swiss National Science Foundation (SNSF) in the frame of the National Centre for Competence in Research PlanetS, and has received funding from the European Research Council (ERC) under the European Union's Horizon 2020 research and innovation programme (project Four Aces; grant agreement No 724427). S.D. acknowledges Vaibhav Pant for insightful discussions.

References

Albrecht, S., Winn, J. N., Marcy, G. W., et al. 2013, *ApJ*, 771, 11
 Allart, R., Lovis, C., Pino, L., et al. 2017, *A&A*, 606, A144
 Baranne, A., Queloz, D., Mayor, M., et al. 1996, *A&AS*, 119, 373
 Bate, M. R., Lodato, G., & Pringle, J. E. 2010, *MNRAS*, 401, 1505
 Batygin & Konstantin. 2012, *Nature*, 491, 418
 Boué, G. & Fabrycky, D. C. 2014, *The Astrophysical Journal*, 789, 111

Boué, G. & Laskar, J. 2006, *Icarus*, 185, 312
 Bourrier, V., Cegla, H. M., Lovis, C., & Wyttenbach, A. 2017, *A&A*, 599, A33
 Bourrier, V. & Hébrard, G. 2014, *A&A*, 569, A65
 Bourrier, V., Lecavelier des Etangs, A., Hébrard, G., et al. 2015, *A&A*, 579, A55
 Bourrier, V., Lovis, C., Beust, H., et al. 2018, *Nature*, 553, 477
 Bouvier, J. 2013, in *EAS Publications Series*, Vol. 62, eprint: arXiv:1307.2891, 143–168
 Cébron, D., Moutou, C., Le Bars, M., Le Gal, P., & Farès, R. 2011, 11, 03003
 Cegla, H. M., Lovis, C., Bourrier, V., et al. 2016a, *A&A*, 588, A127
 Cegla, H. M., Oshagh, M., Watson, C. A., et al. 2016b, *ApJ*, 819, 67
 Christiansen, J. L., Vanderburg, A., Burt, J., et al. 2017, *The Astrophysical Journal*, 154, 122
 Collier Cameron, A., Bruce, V. A., Miller, G. R. M., Triaud, A. H. M. J., & Queloz, D. 2010, *MNRAS*, 403, 151
 Correia, A. C. M. 2015, *A&A*, 582, A69
 Correia, A. C. M., Laskar, J., Farago, F., & Boué, G. 2011, *Celestial Mechanics and Dynamical Astronomy*, 111, 105
 Crouzet, N., McCullough, P. R., Long, D., et al. 2017, *AJ*, 153, 94
 d’Alembert, J. L. R. 1749, *Recherches sur la précession des équinoxes: et sur la nutation de l’axe de la Terre, dans le système newtonien* (Chez David l’aîné)
 Fabrycky, D. & Tremaine, S. 2007, *ApJ*, 669, 1298
 Foreman-Mackey, D., Hogg, D. W., Lang, D., & Goodman, J. 2013, *PASP*, 125, 306
 Gandolfi, D., Barragán, O., Hatzes, A. P., et al. 2017, *AJ*, 154, 123
 Gaudi, B. S. & Winn, J. N. 2007, *ApJ*, 655, 550
 Guillochon, J., Ramirez-Ruiz, E., & Lin, D. 2011, *ApJ*, 732, 74
 Hébrard, G., Bouchy, F., Pont, F., et al. 2008, 409
 Hébrard, G., Lemoine, M., Vidal-Madjar, A., et al. 2002, *ApJS*, 140, 103
 Hirano, T., Narita, N., Sato, B., et al. 2012, *ApJ*, 759, L36
 Huber, D., Carter, J. A., Barbieri, M., et al. 2013, *Science*, 342, 331
 Kamiaka, S., Benomar, O., Suto, Y., et al. 2019, *AJ*, 157, 137
 Kreidberg, L. 2015
 Lai, D., Foucart, F., & Lin, D. N. C. 2011, *MNRAS*, 412, 2790
 Lambeck, K. 1988, *Geophysical Geodesy : The Slow Deformations of the Earth* Lambeck.
 Landin, N. R., Mendes, L. T. S., & Vaz, L. P. R. 2009, *A&A*, 494, 209
 Laskar, J. 1997, *Astronomy and Astrophysics*, 317, L75
 López-Morales, M., Triaud, A. H. M. J., Rodler, F., et al. 2014, *ApJ*, 792, L31
 Marchal, C. & Bozis, G. 1982, *Celestial Mechanics*, 26, 311
 Nagasawa, M., Ida, S., & Bessho, T. 2008, *ApJ*, 678, 498
 Ohta, Y., Taruya, A., & Suto, Y. 2005, *ApJ*, 622, 1118
 Otor, O. J., Montet, B. T., Johnson, J. A., et al. 2016, *AJ*, 152, 165
 Pepe, F., Mayor, M., Rupprecht, G., et al. 2002, *The Messenger*, 110, 9
 Petit, A. C., Laskar, J., & Boué, G. 2018, *Astronomy & Astrophysics*, 617, A93
 Queloz, D., Eggenberger, A., Mayor, M., et al. 2000, *A&A*, 359, L13
 Rodriguez, J. E., Eastman, J. D., Zhou, G., et al. 2019, arXiv e-prints, arXiv:1906.03276
 Sanchis-Ojeda, R., Fabrycky, D. C., Winn, J. N., et al. 2012, *Nature*, 487, 449
 Santerne, A., Hébrard, G., Lillo-Box, J., et al. 2016, *ApJ*, 824, 55
 Tremaine, S. 1991, *Icarus*, 89, 85
 Triaud, A. H. M. J., Collier Cameron, A., Queloz, D., et al. 2010, *A&A*, 524, A25
 Vanderburg, A., Bieryla, A., Duev, D. A., et al. 2016, *ApJ*, 829, L9
 Winn, J. N., Johnson, J. A., Howard, A. W., et al. 2010, *ApJ*, 723, L223
 Yee, S. W., Petigura, E. A., Fulton, B. J., et al. 2018, *AJ*, 155, 255

Appendix A: Details on the three vector model

Appendix A.1: Generic three vector problem

The three vector problem (Boué & Laskar 2006; Boué & Fabrycky 2014) consists in the study of the evolution of the direction of three angular momentum represented by the unit vectors \mathbf{u}_k for $k = 1, 2, 3$ under the equations

$$\begin{aligned} \frac{d\mathbf{u}_1}{dt} &= -\nu^{2/1}(\mathbf{u}_1 \cdot \mathbf{u}_2) \mathbf{u}_2 \times \mathbf{u}_1 - \nu^{3/1}(\mathbf{u}_1 \cdot \mathbf{u}_3) \mathbf{u}_3 \times \mathbf{u}_1 \\ \frac{d\mathbf{u}_2}{dt} &= -\nu^{1/2}(\mathbf{u}_1 \cdot \mathbf{u}_2) \mathbf{u}_1 \times \mathbf{u}_2 - \nu^{3/2}(\mathbf{u}_2 \cdot \mathbf{u}_3) \mathbf{u}_3 \times \mathbf{u}_2 \\ \frac{d\mathbf{u}_3}{dt} &= -\nu^{1/3}(\mathbf{u}_1 \cdot \mathbf{u}_3) \mathbf{u}_1 \times \mathbf{u}_3 - \nu^{2/3}(\mathbf{u}_2 \cdot \mathbf{u}_3) \mathbf{u}_2 \times \mathbf{u}_3. \end{aligned} \quad (\text{A.1})$$

The constant $\nu^{k/j}$ are called the characteristics frequencies and represent the relative influence of the body k over the evolution of j . Their expression depends on the considered problem. The three vector problem is integrable (Boué & Laskar 2006) and the solution is quasiperiodic with two different frequencies. Given an initial state where two vectors are aligned and third is misaligned, it is possible to compute the maximum inclination between the two initially aligned vectors as a function of the initial inclination with the third (Boué & Fabrycky 2014). The maximum inclination depends on the characteristics frequencies and the different cases have been classified in section 5.3 of Boué & Fabrycky (2014).

Appendix A.2: Influence of planet b

In Section 5.1 and 5.2, we claimed that planet b inclination dynamics are most likely governed by the star and only influences planets d and c through a modification of the planet-star coupling. We present here the justification for this assumption as well as details on the expressions of the coupling constants.

Let first focus on the three vector problem ($\mathbf{u}_S, \mathbf{u}_b, \mathbf{u}_d$). For now, we neglect the effect of planet c as we will focus on the dynamics of planet b. Using (Boué & Laskar 2006; Boué & Fabrycky 2014), the characteristic frequencies that appear in equation A.1 have for expression

$$\begin{aligned} \nu^{b/S} &= \frac{\alpha_{Sb}}{S}, & \nu^{d/S} &= \frac{\alpha_{Sd}}{S}, & \nu^{b/d} &= \frac{\beta_{bd}}{G_d} \\ \nu^{S/b} &= \frac{\alpha_{Sb}}{G_b}, & \nu^{S/d} &= \frac{\alpha_{Sd}}{G_d}, & \nu^{d/b} &= \frac{\beta_{bd}}{G_b}, \end{aligned} \quad (\text{A.2})$$

where G_k is the angular momentum of planet k , $S = C_S \omega_S$ is the star rotation angular momentum, with C_S the star moment of inertia and

$$\begin{aligned} \alpha_{Sj} &= \frac{3}{2} \frac{G M_S m_j J_2 R_\star^2}{a_j^3}, \\ \beta_{jk} &= \frac{1}{4} \frac{G m_j m_k a_j}{a_k^2} b_{3/2}^{(1)} \left(\frac{a_j}{a_k} \right). \end{aligned} \quad (\text{A.3})$$

Here α_{Sj} represents the coupling between the star and planet j and β_{jk} the Laplace-Lagrange coupling between planets j and k (we assume $a_j < a_k$). We also define

$$J_2 = \frac{k_2 \omega_S^2 R_\star^3}{3 G M_S}, \quad (\text{A.4})$$

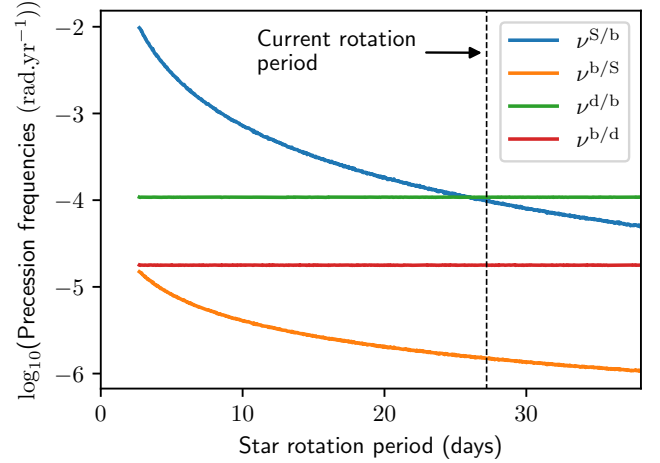


Fig. A.1. Characteristic frequencies defined in Eq. (A.2) as a function of the star period. The current star rotation period is marked with a vertical dashed line. We see that $\nu^{S/b}$ dominates for most of the considered frequencies.

the gravitational quadrupole coefficient (Lambeck 1988), where k_2 is the star's second fluid Love number and ω_S the star rotation speed. For the numerical values of k_2 and C_S , we use (Landin et al. 2009). For a star of mass $0.85 M_\odot$, we have $k_2 = 0.018$ and $C_S/(M_S R_\star^2) = 0.10$.

Independently of the star rotation speed, we have $\alpha_{Sd}/\alpha_{Sb} \leq 0.04$, we therefore neglect the terms depending on α_{Sd} on this analysis. As a result we can directly apply the results of Boué & Fabrycky (2014) analysis, with the four characteristic frequencies $\nu^{b/S}$, $\nu^{S/b}$, $\nu^{b/d}$ and $\nu^{d/b}$.

We plot the frequencies $\nu^{k/j}$ as a function of the stellar period on Figure A.1. We average on each point the frequencies by randomly drawing the orbital elements from the best fit.

We see that for the considered range of star revolution period, $\nu^{S/b}$ dominates all other frequencies and it becomes comparable to $\nu^{d/b}$ for the current rotation rate. Using the regime classification of (Boué & Fabrycky 2014, section 5.3.), we can determine the maximum misalignment between \mathbf{u}_S and \mathbf{u}_b as a function of the initial inclination between \mathbf{u}_S and \mathbf{u}_d .

For a star rotating faster (*i.e.* younger), we have $\nu^{S/b} \gg (\nu^{b/S}, \nu^{d/b}, \nu^{b/d})$, which is a regime where no significant misalignment of planet b can be achieved. As a result, planet b is completely coupled with the star and remains within its equator even if the other planets have a mutual inclination. The current rotation rate leads to the so-called Laplace regime where $(\nu^{S/b} \sim \nu^{d/b}) \gg (\nu^{b/S}, \nu^{b/d})$ in which, planet b plane oscillates between the star equatorial plane and planet d plane. However, if the initial mutual inclination between planet b and the star equator is small, planet b stays close to the star equator.

We simplify the problem by considering that planet b is coupled to the star and modifies the star precession coupling constant α_{Sk} for planets d and c. The modification of the coupling constant can be found in (Boué & Laskar 2006, Eq. 129)³. While the expression was derived in the case of a planet in the presence of a satellite, it remains valid in our

³ The quoted equation actually gives the value of $\tilde{\alpha}_{Sk}/S$ but the computation of $\tilde{\alpha}_{Sk}$ from it is straightforward

case. The expression is a generalization of the approximations for close satellites (Tremaine 1991) and far satellites (d'Alembert 1749). We denote $\tilde{\alpha}_{sk}$ the modified coupling constant to include the effect of planet b considered as a bulge on the star.

Appendix A.3: Coupling constants for the planet interactions with the star

In section 5.2, we consider the three vectors \mathbf{u}_s , \mathbf{u}_d and \mathbf{u}_c . The coupling frequencies that appear in equation (A.1) for this particular problem are given by

$$\begin{aligned} \nu^{d/s} &= \frac{\tilde{\alpha}_{sd}}{S}, & \nu^{c/s} &= \frac{\tilde{\alpha}_{sc}}{S}, & \nu^{d/c} &= \frac{\beta_{dc}}{G_c} \\ \nu^{s/d} &= \frac{\tilde{\alpha}_{sd}}{G_d}, & \nu^{s/c} &= \frac{\tilde{\alpha}_{sc}}{G_c}, & \nu^{c/d} &= \frac{\beta_{dc}}{G_d}, \end{aligned} \quad (\text{A.5})$$

where β_{bd} is defined in Eq. (A.3) and $\tilde{\alpha}_{sk}$ is the coupling between the star and planet k modified to take into account the influence of planet b as explained in section A.2. We also simplify the Eqs. (A.1) by neglecting $\tilde{\alpha}_{sc}$ over $\tilde{\alpha}_{sd}$ since $\tilde{\alpha}_{sc}/\tilde{\alpha}_{sd} < 0.05$ independently of the star rotation period.

Appendix A.4: Coupling constants for the problem with a companion

The characteristic frequencies that govern the evolution of the inclination of the planets under the influence of an outer companion as explained in section 5.3 are given by

$$\begin{aligned} \nu^{\text{pla}/s} &= \frac{\alpha}{S} & \nu^{\text{pla}/\text{comp}} &= \frac{\Gamma}{G'} \\ \nu^{s/\text{pla}} &= \frac{\alpha}{G} & \nu^{\text{comp}/\text{pla}} &= \frac{\Gamma}{G}. \end{aligned} \quad (\text{A.6})$$

where

$$\begin{aligned} \alpha &= \sum_{j=b,c,d} \frac{3}{2} \frac{\mathcal{G} M_s m_j J_2 R_\star^2}{a_j^3} \\ \Gamma &= \sum_{j=b,c,d} \frac{3}{4} \frac{\mathcal{G} m' m_j a_j^2}{b'^3}. \end{aligned} \quad (\text{A.7})$$

We neglect the interaction between the star and the companion and as a result disregard the corresponding characteristic frequencies.

Appendix B: Radial Velocity Data

Table B.1. Radial velocities measured on 2017 November 23 with HARPS-N

BJD	RV (ms ⁻¹)	Uncertainty (ms ⁻¹)
58081.30053	19534.14	1.79
58081.31183	19534.61	1.22
58081.3213	19534.61	2.02
58081.34556	19532.9	0.88
58081.35606	19536.62	0.84
58081.36645	19534.57	0.91
58081.3777	19538.11	0.99
58081.38814	19536.84	0.83
58081.3992	19536.02	0.79
58081.40971	19534.7	0.81
58081.42024	19535.33	0.97
58081.43089	19533.49	1.11
58081.44223	19532.18	0.95
58081.45276	19533.73	0.87
58081.46325	19533.37	0.89
58081.47383	19532.98	0.83
58081.48465	19532.62	0.71
58081.49539	19533.53	0.66
58081.5059	19531.55	0.77
58081.51666	19530.46	1.16
58081.52598	19530.48	1.45
58081.53888	19532.69	2.33
58081.54778	19530.42	1.85
58081.55897	19527.89	2.72